An allosteric network in spastin couples multiple activities required for microtubule severing

Colby R. Sandate [1], Agnieszka Szyk[2], Elena A. Zehr[2], Gabriel C. Lander [1]* and
Antonina Roll-Mecak [2,3]*

The AAA+ ATPase spastin remodels microtubule arrays through severing and its mutation is the most common cause of hereditary spastic paraplegias (HSP). Polyglutamylation of the tubulin C-terminal tail recruits spastin to microtubules and modulates severing activity. Here, we present a ~3.2 Å resolution cryo-EM structure of the *Drosophila melanogaster* spastin hexamer with a polyglutamate peptide bound in its central pore. Two electropositive loops arranged in a double-helical staircase coordinate the substrate sidechains. The structure reveals how concurrent nucleotide and substrate binding organizes the conserved spastin pore loops into an ordered network that is allosterically coupled to oligomerization, and suggests how tubulin tail engagement activates spastin for microtubule disassembly. This allosteric coupling may apply generally in organizing AAA+ protein translocases into their active conformations. We show that this allosteric network is essential for severing and is a hotspot for HSP mutations.

S pastin is a microtubule-severing AAA ATPase (ATPases associated with diverse cellular activities) whose function is important in basic cell biological processes ranging from neurogenesis and axonal maintenance to nuclear envelope breakdown, vesicle trafficking, mitosis and cytokinesis[1]. Spastin is recruited to endosomes and the midbody through its interaction with ESCRTIII and is thought to participate in the coordinated remodeling of membranes and microtubules[1]. Spastin ATPase activity is stimulated by microtubules[2–4] and microtubule severing activity requires adenosine triphosphate (ATP) hydrolysis[2,5–7]. Spastin mutations are responsible for ~50% of hereditary spastic paraplegias (HSPs), a large and clinically diverse family of neurodegenerative disorders[8]. In the pure form of the disease, HSP patients typically exhibit axonal degeneration in motor axons of the corticospinal tract, leading to progressive lower limb spasticity and weakness[8–10]. Studies in model organisms[11] and patient-derived induced pluripotent stem cells[12] have shown that neurons are especially sensitive to spastin gene dosage. Cellular and biochemical studies have shown that many of the disease-associated mutations examined impair microtubule severing and ATP hydrolysis[5–7,13]. However, the etiology of spastin induced HSP is still poorly understood.

Spastin has a modular structure comprising a three-helix bundle microtubule-interacting and trafficking (MIT) domain, a poorly conserved linker region and an AAA+ ATPase domain. This domain architecture is shared among all three known microtubule severing enzymes: spastin, katanin and fidgetin[1]. The ATPase domain is structurally homologous to that of other members of the AAA+ protein family and consists of an α/β nucleotide binding domain (NBD) and a four-helix bundle domain (HBD). Both spastin and katanin differ from other AAA+ ATPase enzymes in that they contain two additional helices within the NBD that are essential for severing[6,14]. The AAA+ ATPase domains hexamerize in a nucleotide-dependent manner and the tubulin substrate lowers the critical concentration for oligomerization[15,16]. Consistent with this, high-affinity binding of spastin to microtubules is highly

cooperative and requires ATP[4]. The substrate-dependent oligomerization is likely important for the specificity and timing of action of these AAA+ ATPases in the cell, as unregulated spastin and katanin microtubule severing activity is highly deleterious[17–19]. The majority of disease-associated mutations of the *SPAST* gene are found in the ATPase domain of spastin.

Microtubule severing by spastin requires the β-tubulin C-terminal tail, an intrinsically disordered element that decorates the microtubule surface. While the α-tubulin tail contributes to binding, it is not required for severing activity[20]. It was proposed that microtubule severing involves the hexamerization of spastin protomers around the ~20 residue negatively charged tubulin tail, and the subsequent pulling of the tubulin subunit out of the microtubule lattice using ATP-driven conformational changes in three pore loops that help translocate the substrate through the central pore of the hexameric ATPase[6,21]. However, there has been no direct demonstration of the tubulin tail engagement by the spastin pore nor any atomistic structural information on the spastin hexamer or its interaction with the tubulin tail substrate. The interaction of spastin with the microtubule is strongly enhanced by the polyglutamylation of the β-tubulin tail[20], a post-translational modification that involves the addition of multiple glutamate chains of variable lengths; unmodified microtubules are not effectively severed at in vivo spastin concentrations[20,22]. As many as 21 glutamates have been detected on tubulin tails in vivo[23,24]. Polyglutamylation is highly abundant in neurons where spastin activity is required for neurite extension as well as axonal maintenance and regeneration[11].

Here, we present the cryo-EM structure of the spastin hexamer in complex with a polyglutamate peptide at ~3.2 Å resolution. The structure reveals an asymmetric hexamer with the AAA domains arranged in a split lock-washer conformation. Two conserved pore loops from the six protomers form a double-helical staircase gripping the odd and even glutamates of the substrate peptide, respectively. Residues in this double helix are positively charged and neutralize the electronegative polyglutamate peptide, consistent

[1]The Scripps Research Institute, La Jolla, CA, USA. [2]Cell Biology and Biophysics Unit, Porter Neuroscience Research Center, National Institute of Neurological Disorders and Stroke, Bethesda, MD, USA. [3]Biochemistry and Biophysics Center, National Heart, Lung and Blood Institute, Bethesda, MD, USA. *e-mail: glander@scripps.edu; antonina@mail.nih.gov

with the regulation of microtubule severing by polyglutamylation of tubulin tails. The substrate binding pore loops are allosterically coupled to the ATP binding site as well as the oligomerization interfaces, providing a structural explanation for the tubulin substrate binding-induced spastin activation. The majority of the residues in this allosteric network are mutated in HSP patients, underscoring their importance to spastin function. Our comprehensive structural analysis of all reported HSP-associated spastin missense mutations in its AAA core provides a framework for understanding spastin molecular dysfunction.

Results

Spastin forms a hexameric spiral. Unlike many AAA+ ATPases, spastin exists as a monomer or dimer in the absence of nucleotide or bound to ADP, and only assembles into hexamers upon ATP binding[3,6] This hexamer is labile and falls apart at lower concentrations[6]. To stabilize the hexameric state for structural studies by cryo-electron microscopy (cryo-EM) we used a commonly used mutation in the Walker B motif of the ATPase domain (E583Q), which retains ATP binding but prevents ATP hydrolysis[6,13]. Analytical ultracentrifugation (AUC) shows that this construct assembles into hexamers in the presence of ATP at concentrations as low as 6 μM (Supplementary Fig. 1a). Initial structure determination yielded a reconstruction of the spastin hexamer limited to ~3.8 Å resolution showing cryo-EM density of adventitious peptide binding. As polyglutamylation enhances substrate binding[20] and spastin has been shown to interact with polyglutamate peptides, we incubated our spastin preparation with polyglutamate (Methods). This increased the proportion of intact hexamers and allowed structural determination of the spastin-peptide complex to ~3.2 Å resolution (Table 1, Fig. 1 and Supplementary Figs. 2 and 3). Polyglutamate activates spastin ATPase with a maximal activation of approximately sixfold above the basal level (Supplementary Fig. 1b), comparable to the activation reported with microtubules[2]. AUC with a fluorescently labeled polyglutamate peptide shows that it comigrates with the spastin hexamer (Supplementary Fig. 1c). The choice of polyglutamate also overcomes the experimental issue of placing enzymes in a specific register with respect to the tubulin tail sequence that is overrepresented in polyglutamates, but also contains other amino acid residues.

The overall architecture of the spastin hexamer resembles that of a split lock-washer, as previously observed for other homohexameric ATPases[25,26], including the related severing enzyme katanin[14] (Fig. 1a). The individual protomers assemble into a right-handed spiral, with a ~6 Å rise for each protomer and a ~35 Å gap between the topmost and lowest protomers. The large (NBD) subdomain of the ATPase forms the central pore of the hexamer, with the HBD directed peripherally and in contact with the NBD of the neighboring protomer. The cryo-EM density corresponding to the 'gating' protomers A and F is lower in resolution (particularly the HBD of protomer F) than that of the central four protomers, indicative of increased flexibility (Supplementary Fig. 3b). The MIT (which is dispensable for microtubule severing activity[13]) and most of the linker are not observed in the reconstruction, and were likely to have been averaged out during image processing due to their conformational variability, as seen for katanin[14]. However, the EM map was of sufficient quality to model 98.7% of the residues in the hexameric ATPase domains (Table 1, Fig. 1b and Supplementary Fig. 4a).

Our reconstruction contains interpretable cryo-EM density features within each of the six nucleotide binding pockets. With the exception of the gating protomer F, all protomers contain a clearly defined ATP molecule with a magnesium ion coordinated between the β- and γ-phosphates and T530 of the phosphate binding loop (Supplementary Fig. 4b). R640 and R641 from the neighboring protomer complete the ATP binding site for all protomers except for the gating protomer F. The Arg finger residue R641 is in a

Table 1 | Cryo-EM data collection, refinement and validation statistics

|	Spastin[E583Q]
	(EMD-20226, PDB 6P07)
Data collection and processing	
Microscope	Thermo Fischer Talos Arctica
Camera	Gatan K2 Summit DED
Magnification (nominal)	×36,000
Magnification (calibrated)	×43,478.3
Voltage (kV)	200
Total electron exposure (e⁻/Å²)	52
Exposure rate (e-/pixel/s)	5.6
Defocus range (μm)	−1.0 to −2.0
Pixel size (Å)	1.15
Micrographs collected (no.)	2,534
Micrographs used (no.)	2,534
Total extracted particles (no.)	2,736,865
Refined particles (no.)	1,259,553
Final particles (no.)	488,385
Symmetry imposed	C1
Resolution (global)	
FSC 0.5 (unmasked/masked)	7.0/3.6
FSC 0.143 (unmasked/masked)	4.3/3.2
Resolution range (local)	3–5
Model composition	
Nonhydrogen atoms	14,089
Protein residues	1804
Ligands	12
Refinement	
Initial model used (PDB code)	3B9P
Average FSC	3.2
B factors (Å²)	
Protein residues	46.8
Ligands	50.5
R.m.s. deviations	
Bond lengths (Å)	0.01
Bond angles (°)	1.14
Validation	
MolProbity score	1.46
Clashscore	3.05
Poor rotamers (%)	0.0
C-beta deviations	0
Mean per-residue Cα r.m.s. deviation (Å)	0.64
Per-residue Cα r.m.s. deviation range (Å)	0.03–5.66
Ramachandran plot	
Favored (%)	94.65%
Allowed (%)	5.35%
Disallowed (%)	0.00%
EMRinger score[69]	3.00
CaBLAM outliers	3.35%
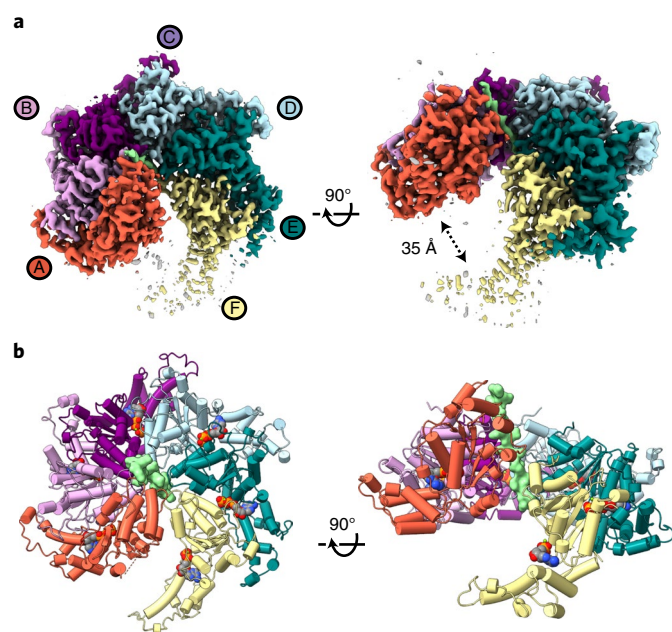
Fig. 1 | The architecture of the substrate-bound spastin hexamer in a split lock-washer conformation. a, Top (left) and side (right) views of the EM map of the spastin hexamer with individual protomers shown in a different color. Substrate density is colored in light green. The ~35 Å gap between protomer A and F is more apparent in the side view. **b,** Top (left) and side (right) views of the atomic model in ribbon representation, with same colors as in panel **a**. Nucleotides are depicted as space-filling models and the polyglutamate peptide substrate is shown in surface representation.

catalytically competent conformation and within H-bonding distance from the γ-phosphate (Supplementary Fig. 4b). The nucleotide binding pocket of protomer F is not as well resolved as in the other protomers (Supplementary Fig. 4b), and the cryo-EM density could correspond to either ADP or ATP. The binding pocket of protomer F is exposed to solution, presumably flexible, and the lack of clear density for the γ-phosphate could arise from either incomplete coordination of the ATP or to background hydrolysis of the ATP. However, a comparison of the overall fold of this F protomer to the ATP-bound protomers (Supplementary Fig. 5a) reveals that their structures are highly similar (0.695 Å Cα r.m.s. deviation). In contrast, comparing the structures of the apo spastin monomer (PDB 3B9P)[6] with the ATP-bound protomers in our structure (Supplementary Fig. 5b) shows extensive conformational rearrangement of the NBD, as well as a ~9° rotation of the HBD relative to the NBD, consistent with nucleotide binding being the main driver of the conformational changes required for hexamerization of the ATPase protomers. Notably, three conserved and functionally important loops in the AAA domain are disordered or poorly ordered in the nucleotide-free structures of spastin[6,27], but are well-ordered in our hexamer structure and line the central pore, where they are involved in substrate binding and interprotomer contacts. Linker residues 455–463 preceding α1 also become ordered in the hexamer and are stabilized through interactions with helix α1 from the neighboring protomer (Supplementary Fig. 6a). Interestingly, the structure of this linker region is distinct from the 'fishhook' motif found in katanin, which decorates the N-terminal side of the central pore and also participates in protomer-protomer contacts[14]. Helix α1 is unique to severing enzymes and mutations in this helix impair severing[6]. The linker connecting helices α1 and α2 moves in concert with the closure of the NBD and HBD around the nucleotide, establishing stabilizing interactions with the α1–β4 loop of the neighboring lower protomer. The latter loop is disordered in the

apo structure[6]. On the opposite face of the hexamer, the C terminus of the AAA domain (residues 753–757), which is disordered in prior crystal structures[6,27], is engaged in intimate contacts with the α10–α11 loop of the neighboring protomer (Supplementary Fig. 6b) and together with helix α11 forms a belt around the hexamer as in katanin[14]. Invariant Y753 at the end of helix α11 is part of the interface with the α11–α12 linker of the neighboring protomer (Supplementary Fig. 6c) and its mutation severely impairs severing[6].

A double-helical staircase of pore loops coordinates the substrate. Density for the polyglutamate peptide is clearly visible at the center of the spastin hexamer (Fig. 2). While the added polyglutamate peptide ranges in length from 10 to 37 amino acids, only the 15 residues that undergo stabilizing interactions with the spastin AAA core are clearly visible (Fig. 2a,b and Fig. 3a). We were unable to assign the polarity of the substrate peptide in the cryo-EM density with certainty at this resolution, as both polarities resulted in acceptable fits to the map (Supplementary Fig. 7) and neither orientation resulted in an increase in stabilizing interactions with the spastin hexamer. We modeled the polarity of the peptide with the N terminus of the peptide engaged to the uppermost protomer (protomer A) and the C terminus closest to the lowest protomer (protomer F). We note that structural and functional studies have so far been unable to unambiguously assign the polarity of the substrate peptide for the meiotic class of AAA ATPases to which spastin and katanin belong, and the current assigned polarity has been inferred from functional studies and analogy with other AAA+ ATPases, including VPS4 (ref. [28]), HSP104 (ref. [29]) and the proteasome[30]. Interestingly, a recent study of the AAA ATPase VAT shows that it is able to translocate peptides in either direction[31]. It is possible that the polarity of the peptide through the spastin pore is not dictated by pore interactions alone and also results from the engagement of other interfaces with the microtubule substrate.

Consistent with the cryo-EM structures of other AAA+ ATPases, pore loop 1 (555–562), which is characterized as having a conserved aromatic residue important for substrate translocation[32], interacts directly with the bound substrate (Fig. 2b and Fig. 3a,b)[28,30,33–35]. Conserved Y556 intercalates between n and $n+2$ residues of the substrate, sandwiching the glutamate sidechain and forming a hydrogen bond with one of the carboxyl oxygens (Fig. 3a,b). Consistent with its role in substrate engagement, its mutation abolishes severing while retaining full ATPase activity (Fig. 4). This intercalating organization between pore loops and substrate has been previously observed in other ATPases[28,29,33] and likely serves as a general mode of substrate interaction for AAA+ ATPases.

Together with invariant K555, which forms a salt bridge with the glutamate of the $n+1$ substrate residue, Y556 constitutes the first of two pore-loop spiral staircases that coordinate the substrate. The sidechain of pore loop 1 residue K555 is also likely stabilized by a hydrogen bond with conserved E462 in helix α1, the secondary structure element unique to severing enzymes[6,14]. VPS4, the other member of the meiotic clade of AAA ATPases, has a short β-strand at this location[36]. Mutation of residues in α1 impair severing without a notable effect on ATPase activity[6]. Invariant H596 and R601 of pore loop 2 (594–601) form electrostatic interactions with every other peptide sidechain substrate (n, $n+2$), generating a second spiral staircase (Fig. 2b and Fig. 3b). Mutation of either of these residues inactivates severing and impairs ATPase activity[6]. Together, pore loops 1 and 2 enclose the polyGlu substrate with a double helix of positively charged residues (Figs. 2b and 3b), neutralizing the highly negative charge of the peptide and providing substrate specificity for either the polyGlu chains on the tubulin tails, or the β-tubulin tails themselves, which contain a high density of negatively charged residues (8–10 glutamates in addition to 2–3 aspartates)[37]. This double coordination by both pore loop 1 and 2 is distinct from VPS4, whose pore loop 2 does not directly contact its polypeptide substrate[28]. Participation of pore loop 2 in substrate translocation has been previously inferred from crosslinking studies
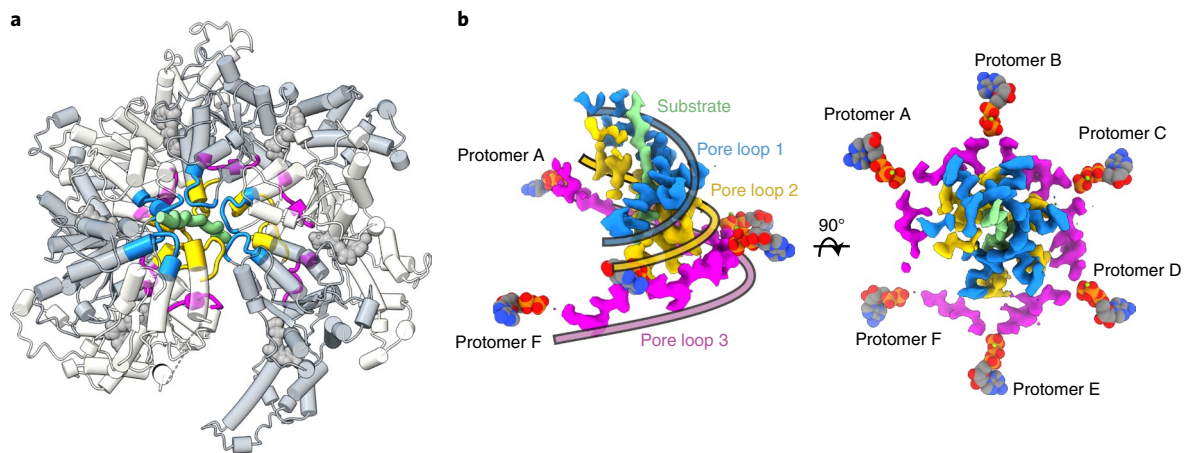
Fig. 2 | A double-helical staircase of pore loops surrounds the substrate and is coupled by a third pore loop spiral to the ATP binding site. a, The three solvent exposed pore loops highlighted on the spastin hexamer structure. Pore loop 1 is colored in blue, pore loop 2 in gold and pore loop 3 in magenta. **b**, Side (left) and top (right) views of the EM density of the triple spiral staircase generated by pore loops 1, 2 and 3. Pore loops 1 and pore loops 2 form a tight double spiral that engages with the peptide substrate (shown in light green). Pore loops 3 form a shallow spiral between pore loops 1–2 and the nucleotide. Ribbons colored as their corresponding pore loops are overlaid on the EM map to highlight the trajectory of the three pore loop spirals.
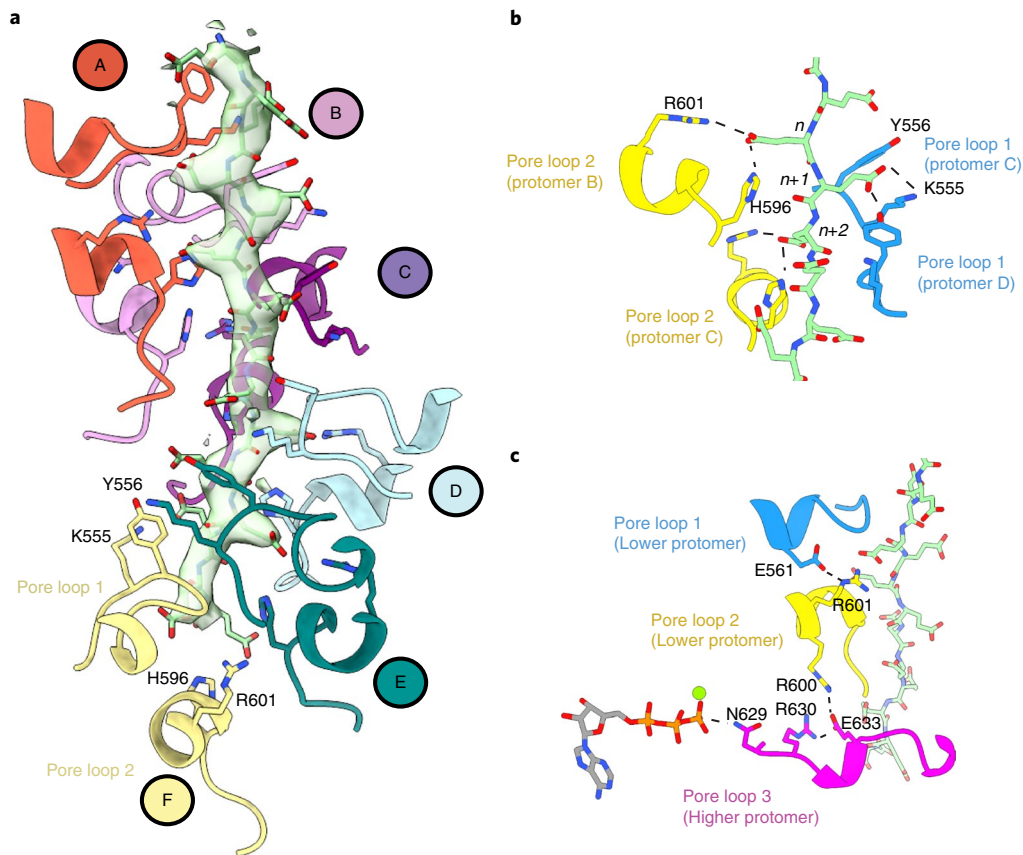
Fig. 3 | A pore loop network couples nucleotide binding to substrate engagement and oligomerization. a, Pore loops 1 and 2 interacting with the polyglutamate substrate. Substrate density is shown as a transparent surface with the polyglutamate model in light green. Pore loops are colored according to their assigned protomer, as in Fig. 1. Residues that interact directly with the substrate (K555, Y556, H596 and R601) are shown in stick representation. **b**, Interactions between the substrate and conserved residues in pore loops 1 and 2. **c**, A network of interactions between charged residues connects the peptide substrate to the nucleotide. Hydrogen bonds are shown as dashed lines. All interactions depicted have a measured distance of less than 4 Å.

of ClpA[38], where mutagenesis of certain residues within the loop inhibits substrate degradation but not substrate binding. Additionally, crystallographic studies of HSP104 show pore loop 2 interacting with an adjacent N′ domain molecule, acting as a 'substrate mimic'[39].

An allosteric network mutated in HSP couples substrate binding to oligomerization. A third highly conserved pore loop in the AAA domain (629–637) runs nearly orthogonal to pore loop 2 and does not contact the substrate peptide directly, but functions as a
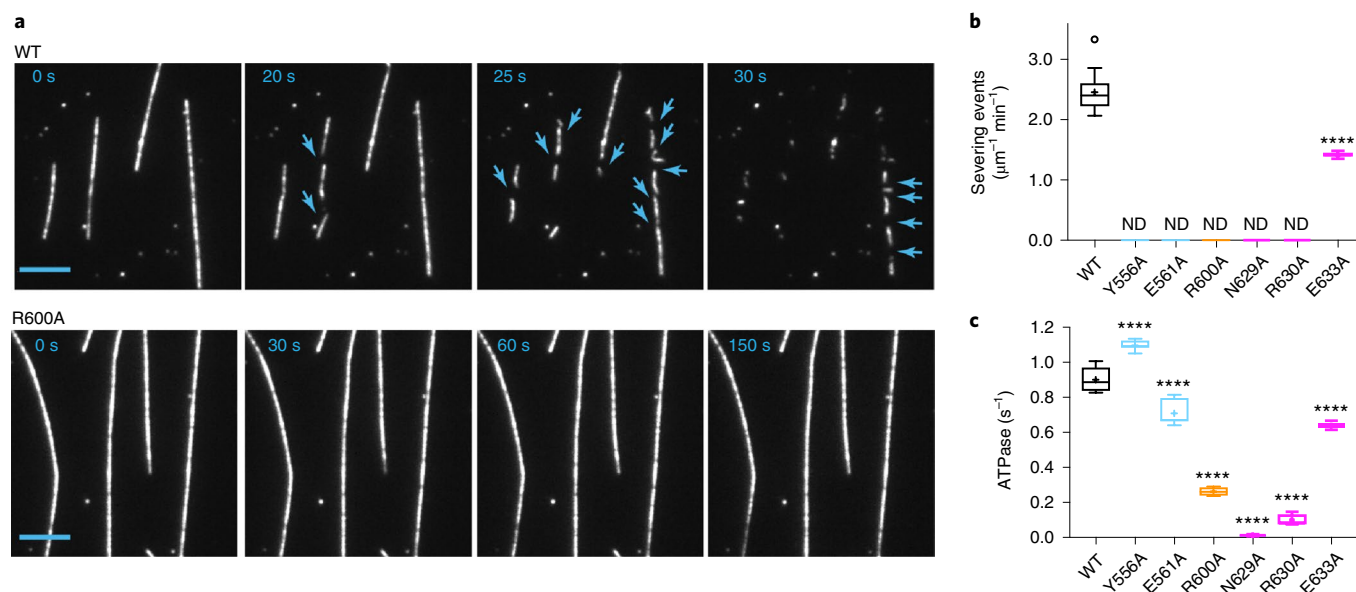
Fig. 4 | Mutations in the three pore loops impair ATPase and microtubule severing. a, Microtubule severing assays of wild-type (WT) spastin and pore loop mutant R600A. Severing events are highlighted with blue arrows. Scale bar, 5 μm. **b**, Tukey plots of severing rates of spastin WT and mutants. $n = 30$ microtubules from 2, 4, 4, 4, 4, 4 and 3 chambers for WT, Y556A, E561A, R600A, E629A, R630A and E633A mutants, respectively. **c**, Tukey plots of ATPase rates of spastin WT and mutants, $n = 24$, 16, 12, 8, 8, 7 and 8 independent measurements for WT, Y556A, E561A, R600A, E629A, R630A and E633A mutants, respectively. For plots in panels **b** and **c**, plus sign denotes mean, box, 25th to 75th percentile, whiskers 1.5× interquartile (IQR) or the smallest (bottom) or largest (top) data point if less than 1.5× IQR, outliers shown as circles. ****$P < 0.0001$, determined by the Mann–Whitney test. ND, not detectable. Pore loop 1, 2 and 3 mutants shown in cyan, orange and magenta, respectively.

structural bridge linking the substrate-interacting pore loops to the nucleotide binding pocket (Fig. 3c). Invariant E561 in α4, which immediately follows pore loop 1, is within proximity of H-bonding interactions, with invariant R601 from pore loop 2 of the same protomer, potentially allowing direct coordination between these two pore loops. Pore loop 2 is disordered in crystal structures of the apo spastin monomer[6,27] (Supplementary Fig. 5b) and the fact that we observe direct interactions between R601 and substrate strongly suggests that the E561-R601 interaction depends on the presence of substrate. Consistent with this role, mutation of E561 abolishes severing, while still retaining ATPase activity (Fig. 4b,c). R601 is also within H-bonding distance to S599 of the lower neighboring protomer, thus possibly linking substrate binding to oligomerization (Supplementary Fig. 6d). Both S599 and R601 are mutated in HSP (Supplementary Table 1) and the R601L disease mutation impairs ATPase and abolishes microtubule severing[6]. The organization of these pore loops gives rise to an interaction network wherein invariant R600 of pore loop 2 forms a salt bridge with invariant E633 in pore loop 3 of the next lower protomer, which in turn interacts with invariant R630 which H-bonds with the backbone of R591 in loop 2 of the upper protomer (Fig. 3c). Invariant N629 in pore loop 3 is within H-bonding distance from the γ-phosphate of the ATP of the same protomer and thus can potentially contribute to nucleotide sensing in addition to the traditional sensor residues. Consistent with this, mutation of N629 abolishes both ATPase activity and severing (Fig. 4b,c). Together with invariant D585, N629 is also within H-bonding distance of invariant R591 of the neighboring lower protomer, which in turn is within hydrogen bonding distance to the catalytic glutamate in the Walker B motif (E583) of the higher protomer (Fig. 5a). The R591 backbone is also stabilized through interaction with the R630 sidechain from the lower protomer (Fig. 5b). Thus, R591 is at the center of an allosteric network that can couple the substrate binding loops to ATP hydrolysis and oligomerization. Moreover, the conformation of pore loop 3 containing R630 is coupled through a network of hydrophobic residues to

helix α11 involved in oligomerization interactions between HBD domains (Fig. 5b and Supplementary Fig. 6b). Mutation of Y753 at this oligomerization interface severely impairs severing[6]. Strikingly, all residues in this extensive network are mutated in HSP patients, highlighting their importance for spastin function (Fig. 5 and Supplementary Table 1). Thus, our structure sheds light on how ATP and peptide substrate binding establish a network of intra- and interprotomer interactions that stabilize the spastin hexamer. Since spastin intracellular concentrations are below the critical concentration for hexamer assembly[6,22], we speculate that this pore loop network primes spastin for assembly around the tubulin tails for effective microtubule severing.

Effect of HSP mutations on spastin activity. There are over 200 HSP-associated spastin mutations reported to date and 30% of them are missense mutations[10]. The majority of spastin missense mutations linked to HSP are located within the ATPase domain[10], and several missense disease mutations examined have been shown to inactivate or severely impair microtubule severing activity in biochemical and cellular studies[5–7,10,13,40]. Our structure provides a mechanistic understanding of how HSP mutations in the ATPase domain lead to loss of spastin function. Based on the high sequence identity and known structural conservation between *Drosophila* and human spastin[6,27], we generated a homology model of the human spastin hexamer (Fig. 6a) that provides complete coverage of the highly conserved AAA domain (amino acids 89–388). Structural analysis of all known missense spastin mutations identified to date in the AAA core[6,41–61] suggests that most impair oligomerization, nucleotide binding, or disrupt the folding or stability of the AAA domain's structure to variable degrees (Supplementary Table 1). Several mutations map directly to the nucleotide binding pocket (Fig. 6b) and impair nucleotide binding (I344K, G385W, N386K, K388R, M390V and R498S) and thus hexamerization. One mutation interferes with magnesium coordination (D441G). Two disease mutations affect ATP hydrolysis and sensing of the γ-phosphate
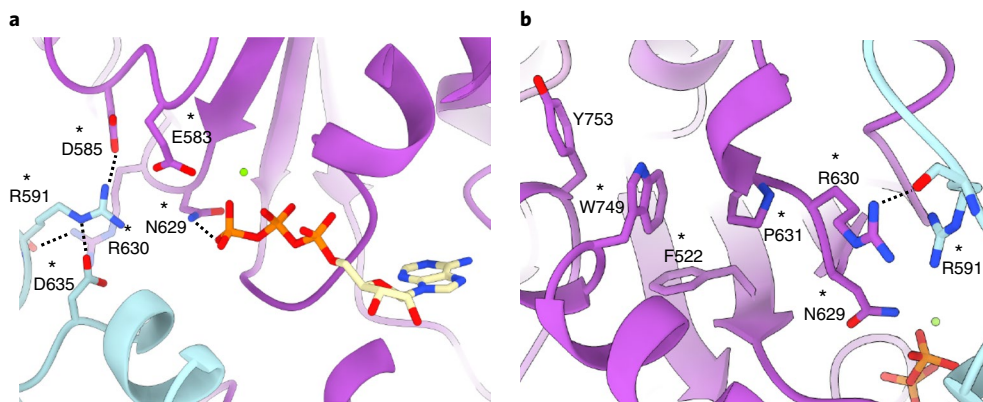
Fig. 5 | An allosteric network mutated in HSP couples substrate binding to oligomerization and ATP hydrolysis. a, Interaction network centered on R591. Residues colored purple and cyan for protomers C and D, respectively. Residues mutated in HSP are indicated with an asterisk. All interactions depicted have a measured distance of less than 4 Å. **b,** W749 makes van der Walls contacts with several hydrophobic residues mutated in HSP and connects pore loop 3 to the C-terminal helix α11 involved in oligomerization. Residues are colored purple and cyan for protomers C and D, respectively. Residues mutated in HSP are indicated with an asterisk. All interactions depicted have a measured distance of less than 4 Å.
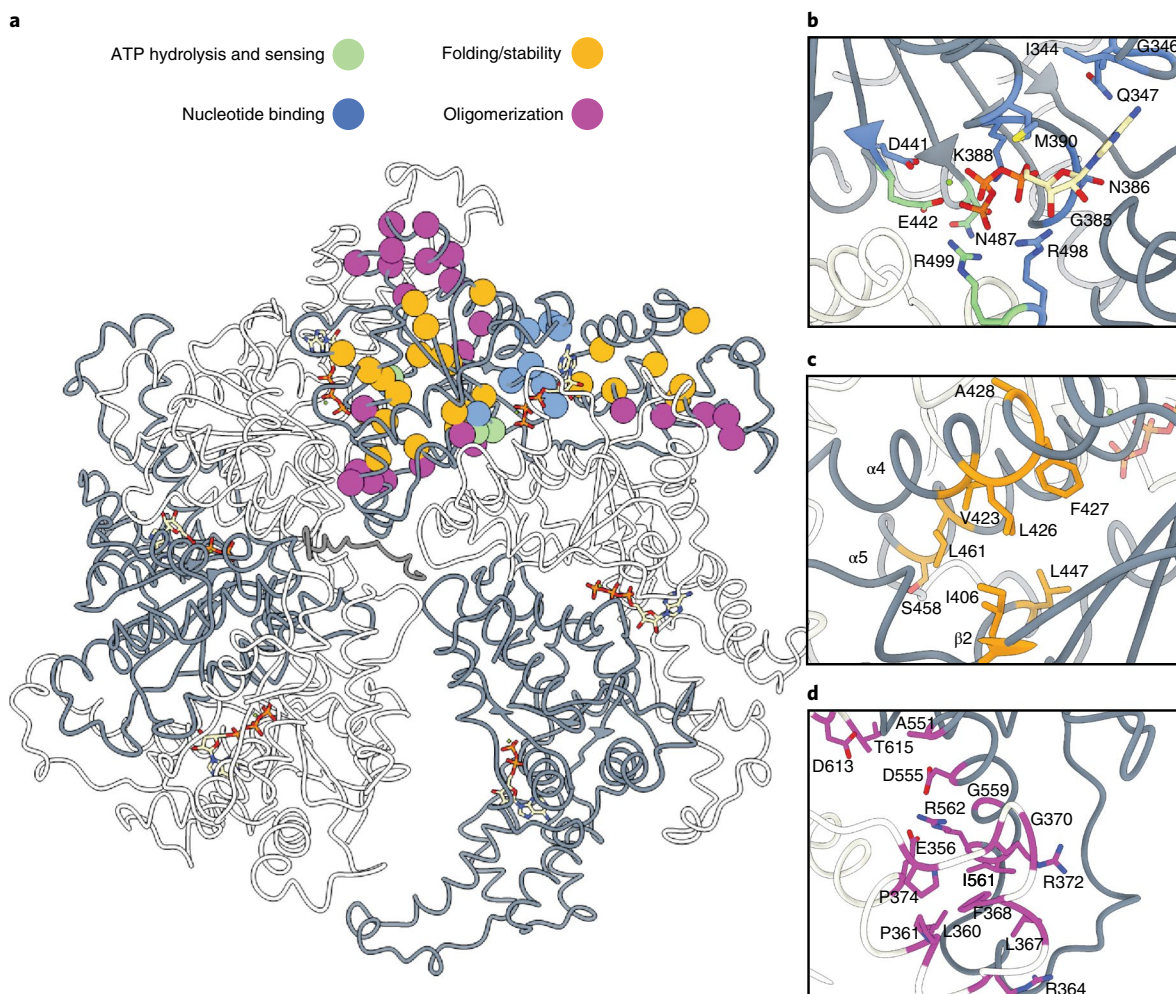
Fig. 6 | Structure-based insight into the mechanism of action of human spastin HSP disease mutations. a, Homology model of the human spastin hexamer depicting the location of missense mutations identified in HSP. Protomers are colored in alternating grey and white around the hexamer. Mutations are depicted as spheres at their Cα position and colored according to their proposed mechanism of action: interference with nucleotide binding (blue), defects in ATP hydrolysis and γ-phosphate sensing (green), disruption of interactions important for folding or conferring stability to the protomer (orange) and disruption of oligomerization interfaces (magenta). **b,** Close-up view of the nucleotide pocket, showing a large number of mutations that likely disrupt nucleotide binding or impair ATP hydrolysis and sensing. **c,** Close-up view of hydrophobic interfaces between α4, α5 and β2 highlighting potentially destabilizing HSP mutations. **d,** Close-up view of the NBD-HBD interaction interface between protomers showing a high density of HSP mutations.

(E442A or K, and R499C). E442 is part of the Walker B motif and participates in catalysis in all AAA ATPases, while R499 serves as the Arg finger. The Arg finger coordinates the γ-phosphate and electrostatically stabilizes the transition state after ATP hydrolysis. N487D (N629 in our *Drosophila* cryo-EM structure) is likely involved in both sensing the γ-phosphate and oligomerization interactions (Figs. 6b and 5a).

Other HSP mutations are likely deleterious because they disrupt the overall fold and stability of the AAA domain structure (Fig. 6c) (I406V, V423L, L426V, F427C, A428P, L447V, S458R and L461P among others). A large number of disease mutations map to protomer-protomer interfaces and likely interfere with oligomerization (Fig. 6d) (E356G, L360P, P361L/S, R364M, L367S, F368L/S, G370R, R372G, C448Y, A551P/Y, D555G/N, E356V, G559D, I561G, R562Q, D613H and T615I). Consistent with this, cellular studies have shown that the C448Y mutant is unable to associate with wild-type spastin and inhibit microtubule severing[62]. Thus, the preponderance of HSP mutations likely impact oligomerization interfaces or the overall stability of spastin and may lead to spastin haploinsufficiency. However, there is a large phenotypic variability in spastin-linked HSP and more recent work has shown that some spastin disease mutations can also have a toxic gain-of-function that is further exacerbated by spastin haploinsufficiency[63]. We note that spastin mutants that are deficient in oligomerization could still bind microtubules through a stretch of residues in the linker that connects the AAA and MIT[3,6,7,13,64] domains and thus have a toxic gain-of-function on the microtubule cytoskeleton. Interestingly, mutations in the Arg finger R499 have been associated with early onset HSP[41,52,53,59,65–68], possibly suggesting a dominant negative effect of this mutation. The Walker B residue E442 is the other strong candidate for a dominant negative mechanism, however not enough phenotypic data are currently available for this HSP mutation. Our structure will serve as a platform for the analysis of HSP mutations and the correlation between genotype and molecular phenotype.

Discussion
Recent cryo-EM studies of AAA+ ATPase protein translocases have shown how a conserved mechanistic infrastructure can be generally utilized for effective nucleotide-driven protein translocation, while also highlighting the allosteric diversity of this family of ATPases. Even within the meiotic clade of AAA+ ATPases, we observe differences in structural motifs such as the substrate-interacting pore loops. For example, while spastin surrounds its substrate through a network of interactions that utilizes both pore loops, the closely related family member VPS4 primarily interacts with the translocating substrate *via* an aromatic-containing pore loop 1, without direct interactions from pore loop 2. Such differences may evolve to accommodate substrate specificity or to modulate the force exerted upon a targeted polypeptide.

Given its structural homology to the C-terminal AAA domain of spastin, it is possible that the katanin ATPase establishes a nucleotide-substrate interaction network that operates under a homologous allosteric mechanism. However, in contrast to previous structural studies of katanin, we only observed the split lock-washer conformation of spastin and were unable to identify a closed-ring conformer within our datasets as observed for other AAA ATPases, including the closely related meiotic clade members katanin[14] and VPS4 (ref. [28]). One possible explanation for this could be a higher ATP binding affinity for spastin versus katanin, which could prevent the dissociation of nucleotide in protomer F under our experimental conditions, a requirement for adoption of the closed-ring conformation previously observed for katanin[14] and VPS4 (ref. [28]). We speculate that the split lock-washer conformation of spastin observed here represents a pre-hydrolysis state where all six protomers are engaged with the substrate peptide.

In summary, our structure of spastin elucidates the details of substrate engagement by a microtubule severing enzyme and reveals how three conserved pore loops in spastin establish a conduit that links substrate binding with oligomerization and ATP hydrolysis. Our comprehensive analysis of human HSP mutations reveals the extensive coverage of disease mutations on the spastin hexamer and how they would impact all major facets of hexamer function: ATP binding, hydrolysis and oligomerization.

Online content
Any methods, additional references, Nature Research reporting summaries, source data, statements of code and data availability and associated accession codes are available at https://doi.org/10.1038/s41594-019-0257-3.

References
1. Mcnally F. J., & Roll-Mecak A. Microtubule-severing enzymes: from cellular functions to molecular mechanism. *J. Cell Biol.* **217**, 4057 (2018).
2. Salinas, S. et al. Human spastin has multiple microtubule-related functions. *J. Neurochem.* **95**, 1411–1420 (2005).
3. Eckert, T. et al. Spastin's microtubule-bnding properties and comparison to katanin. *PLoS ONE* **7**, 1–16 (2012).
4. Wen, M. & Wang, C. The nucleotide cycle of spastin correlates with its microtubule-binding properties. *FEBS J.* **280**, 3868–3877 (2013).
5. Evans, K. J., Gomes, E. R., Reisenweber, S. M., Gundersen, G. G. & Lauring, B. P. Linking axonal degeneration to microtubule remodeling by Spastin-mediated microtubule severing. *J. Cell Biol.* **168**, 599–606 (2005).
6. Roll-Mecak, A. & Vale, R. D. Structural basis of microtubule severing by the hereditary spastic paraplegia protein spastin. *Nature* **451**, 363–367 (2008).
7. Roll-Mecak, A. & Vale, R. D. The Drosophila homologue of the hereditary spastic paraplegia protein, spastin, severs and disassembles microtubules. *Curr. Biol.* **15**, 650–655 (2005).
8. Hazan, J. et al. Spastin, a new AAA protein, is altered in the most frequent form of autosomal dominant spastic paraplegia. *Nat. Genet.* **23**, 296–303 (1999).
9. Blackstone, C., O'Kane, C. J. & Reid, E. Hereditary spastic paraplegias: membrane traffic and the motor pathway. *Nat. Rev. Neurosci.* **12**, 31–42 (2011).
10. Solowska, J. M. & Baas, P. W. Hereditary spastic paraplegia SPG4: what is known and not known about the disease. *Brain* **138**, 2471–2484 (2015).
11. Stone, M. C. et al. Normal spastin gene dosage Is specifically required for axon regeneration. *Cell Rep.* **2**, 1340–1350 (2012).
12. Havlicek, S. et al. Gene dosage-dependent rescue of HSP neurite defects in SPG4 patients' neurons. *Hum. Mol. Genet.* **23**, 2527–2541 (2014).
13. White, S. R., Evans, K. J., Lary, J., Cole, J. L. & Lauring, B. Recognition of C-terminal amino acids in tubulin by pore loops in Spastin is important for microtubule severing. *J. Cell Biol.* **176**, 995–1005 (2007).
14. Zehr, E. et al. Katanin spiral and ring structures shed light on power stroke for microtubule severing. *Nat. Struct. Mol. Biol.* **24**, 717–725 (2017).
15. Hartman, J. J. & Vale, R. D. Microtubule disassembly by ATP-dependent oligomerization of the AAA enzyme katanin. *Science* **286**, 782–785 (1999).
16. Eckert, T. et al. Subunit interactions and cooperativity in the microtubule-severing AAA ATPase spastin. *J. Biol. Chem.* **287**, 26278–26290 (2012).
17. Cummings, C. M., Bentley, C. A., Perdue, S. A., Baas, P. W. & Singer, J. D. The Cul3/Klhdc5 E3 ligase regulates p60/katanin and is required for normal mitosis in mammalian cells. *J. Biol. Chem.* **284**, 11663–11675 (2009).
18. Lu, C., Srayko, M. & Mains, P. E. The *Caenorhabditis elegans* microtubule-severing complex MEI-1/MEI-2 katanin interacts differently with two superficially redundant β-tubulin isotypes. *Mol. Biol. Cell* **15**, 142–150 (2004).
19. Sherwood, N. T., Sun, Q., Xue, M., Zhang, B. & Zinn, K. Drosophila spastin regulates synaptic microtubule networks and is required for normal motor function. *PLoS Biol.* **2**, e429 (2004).
20. Valenstein, M. L. & Roll-Mecak, A. Graded control of microtubule severing by tubulin glutamylation. *Cell* **164**, 911–921 (2016).
21. Vemu, A. et al. Severing enzymes amplify microtubule arrays through lattice GTP-tubulin incorporation. *Science* **361**, eaau1504 (2018).
22. Itzhak, D. N., Tyanova, S., Cox, J. & Borner, G. H. H. Global, quantitative and dynamic mapping of protein subcellular localization. *eLife* **5**, 1–36 (2016).
23. Geimer, S., Teltenkötter, A., Plessmann, U., Weber, K. & Lechtreck, K. F. Purification and characterization of basal apparatuses from a flagellate green alga. *Cell Motil. Cytoskelet.* **37**, 72–85 (1997).
24. Schneider, A., Plessmann, U., Felleisen, R. & Weber, K. Posttranslational modifications of trichomonad tubulins; identification of multiple glutamylation sites. *FEBS Lett.* **429**, 399–402 (1998).

25. Abid Ali, F. et al. Cryo-EM structures of the eukaryotic replicative helicase bound to a translocation substrate. *Nat. Commun.* **7**, 10708 (2016).

26. Skordalakes, E. & Berger, J. M. Structure of the Rho transcription terminator: mechanism of mRNA recognition and helicase loading. *Cell* **114**, 135–146 (2003).

27. Taylor, J. L., White, S. R., Lauring, B. & Kull, F. J. Crystal structure of the human spastin AAA domain. *J. Struct. Biol.* **179**, 133–137 (2012).

28. Han, H. et al. binds ESCRT-III substrates through a repeating array of dipeptide-binding pockets. *eLife* **6**, 1–15 (2017).

29. Gates, S. N. et al. Ratchet-like polypeptide translocation mechanism of the AAA+ disaggregase Hsp104. *Science* **357**, 273–279 (2017).

30. De la Peña, A. H., Goodall, E. A., Gates, S. N., Lander, G. C. & Martin, A. Substrate-engaged 26S proteasome structures reveal mechanisms for ATP-hydrolysis–driven translocation. *Science* **362**, eaav0725 (2018).

31. Augustyniak, R. & Kay, L. E. Cotranslocational processing of the protein substrate calmodulin by an AAA+ unfoldase occurs via unfolding and refolding intermediates. *Proc. Natl Acad. Sci. USA* **115**, E4786–E4795 (2018).

32. Schlieker, C. et al. Substrate recognition by the AAA+ chaperone ClpB. *Nat. Struct. Mol. Biol.* **11**, 607–615 (2004).

33. Puchades, C. et al. Structure of the mitochondrial inner membrane AAA+ protease YME1 gives insight into substrate processing. *Science* **358**, eaao0464 (2017).

34. Ripstein, Z. A., Huang, R., Augustyniak, R., Kay, L. E. & Rubinstein, J. L. Structure of a AAA+ unfoldase in the process of unfolding substrate. *eLife* **6**, 1–14 (2017).

35. Alfieri, C., Chang, L. & Barford, D. Mechanism for remodelling of the cell cycle checkpoint protein MAD2 by the ATPase TRIP13. *Nature* **559**, 274–278 (2018).

36. Scott, A. et al. Structural and mechanistic studies of VPS4 proteins. *EMBO J.* **24**, 3658–3669 (2005).

37. Roll-Mecak, A. Intrinsically disordered tubulin tails: complex tuners of microtubule functions? *Semin. Cell Dev. Biol.* **37**, 11–19 (2015).

38. Hinnerwisch, J., Fenton, W. A., Furtak, K. J., Farr, G. W. & Horwich, A. L. Loops in the central channel of ClpA chaperone mediate protein binding, unfolding, and translocation. *Cell* **121**, 1029–1041 (2005).

39. Lee, J. et al. Structural determinants for protein unfolding and translocation by the Hsp104 protein disaggregase. *Biosci. Rep.* **37**, BSR20171399 (2017).

40. Charvin, D. et al. Mutations of SPG4 are responsible for a loss of function of spastin, an abundant neuronal protein localized in the nucleus. *Hum. Mol. Genet.* **12**, 71–78 (2003).

41. Mészárosová, A. U. et al. SPAST mutation spectrum and familial occurrence among Czech patients with pure hereditary spastic paraplegia. *J. Hum. Genet.* **61**, 845–850 (2016).

42. Ishiura, H. et al. Molecular epidemiology and clinical spectrum of hereditary spastic paraplegia in the Japanese population based on comprehensive mutational analyses. *J. Hum. Genet.* **59**, 163–172 (2014).

43. Depienne, C. et al. Spastin mutations are frequent in sporadic spastic paraparesis and their spectrum is different from that observed in familial cases. *J. Med. Genet.* **43**, 259–265 (2006).

44. Tang, B. S. et al. Clinical features of hereditary spastic paraplegia with thin corpus callosum: report of 5 Chinese cases. *Chin. Med. J. (Engl.)* **117**, 1002–1005 (2004).

45. Hentati, A. et al. Novel mutations in spastin gene and absence of correlation with age at onset of symptoms. *Neurology* **55**, 1388–1390 (2000).

46. Meijer, I. A., Hand, C. K., Cossette, P., Figlewicz, D. A. & Rouleau, G. A. Spectrum of SPG4 mutations in a large collection of North American families with hereditary spastic paraplegia. *Arch. Neurol.* **59**, 281–286 (2002).

47. Patrono, C. et al. Autosomal dominant hereditary spastic paraplegia: DHPLC-based mutation analysis of SPG4 reveals eleven novel mutations. *Hum. Mutat.* **25**, 506 (2005).

48. Balicza, P. et al. Genetic background of the hereditary spastic paraplegia phenotypes in Hungary - An analysis of 58 probands. *J. Neurol. Sci.* **364**, 116–121 (2016).

49. Bürger, J. et al. Hereditary spastic paraplegia caused by mutations in the SPG4 gene. *Eur. J. Hum. Genet.* **8**, 771–776 (2000).

50. Elert-Dobkowska, E. et al. Molecular spectrum of the SPAST, ATL1 and REEP1 gene mutations associated with the most common hereditary spastic paraplegias in a group of Polish patients. *J. Neurol. Sci.* **359**, 35–39 (2015).

51. Lu, X. et al. Genetic analysis of SPG4 and SPG3A genes in a cohort of Chinese patients with hereditary spastic paraplegia. *J. Neurol. Sci.* **347**, 368–371 (2014).

52. Park, H. et al. Mutational spectrum of the SPAST and ATL1 genes in Korean patients with hereditary spastic paraplegia. *J. Neurol. Sci.* **357**, 167–172 (2015).

53. Polymeris, A. A. et al. A series of Greek children with pure hereditary spastic paraplegia: clinical features and genetic findings. *J. Neurol.* **263**, 1604–1611 (2016).

54. Aulitzky, A. et al. A complex form of hereditary spastic paraplegia in three siblings due to somatic mosaicism for a novel SPAST mutation in the mother. *J. Neurol. Sci.* **347**, 352–355 (2014).

55. McDermott, C. J. et al. Clinical features of hereditary spastic paraplegia due to spastin mutation. *Neurology* **67**, 45–51 (2006).

56. Yabe, I., Sasaki, H. & Tashiro, K. Spastin gene mutation in Japanese with hereditary spastic paraplegia. *J. Med.* **39**, 14–15 (2002).

57. Dong, E. L. et al. Clinical spectrum and genetic landscape for hereditary spastic paraplegias in China. *Mol. Neurodegener.* **13**, 1–14 (2018).

58. Luo, Y. et al. A diagnostic gene chip for hereditary spastic paraplegias. *Brain Res. Bull.* **97**, 112–118 (2013).

59. Shoukier, M. et al. Expansion of mutation spectrum, determination of mutation cluster regions and predictive structural classification of SPAST mutations in hereditary spastic paraplegia. *Eur. J. Hum. Genet.* **17**, 187–194 (2009).

60. Fonknechten, N. et al. Spectrum of SPG4 mutations in autosomal dominant spastic paraplegia. *Hum. Mol. Genet.* **9**, 637–644 (2000).

61. Proukakis, C., Moore, D., Labrum, R., Wood, N. W. & Houlden, H. Detection of novel mutations and review of published data suggests that hereditary spastic paraplegia caused by spastin (SPAST) mutations is found more often in males. *J. Neurol. Sci.* **306**, 62–65 (2011).

62. Solowska, J. M. et al. Pathogenic Mutation of Spastin Has Gain-of-Function Effects on Microtubule Dynamics. *J. Neurosci.* **34**, 1856–1867 (2014).

63. Qiang, L. et al. Hereditary spastic paraplegia: gain-of-function mechanisms revealed by new transgenic mouse. *Hum. Mol. Genet.* **28**, 1136–1152 (2018).

64. Errico, A., Ballabio, A. & Rugarli, E. I. Spastin, the protein mutated in autosomal dominant hereditary spastic paraplegia, is involved in microtubule dynamics. *Hum. Mol. Genet.* **11**, 153–163 (2002).

65. Crippa, F. et al. Eight novel mutations in SPG4 in a large sample of patients with hereditary spastic paraplegia. *Arch. Neurol.* **63**, 750–755 (2006).

66. França, M. C. et al. SPG4-related hereditary spastic paraplegia: frequency and mutation spectrum in Brazil. *Clin. Genet.* **86**, 194–196 (2014).

67. Kim, T.-H. et al. Mutation analysis of SPAST, ATL1, and REEP1 in Korean patients with hereditary spastic paraplegia. *J. Clin. Neurol.* **10**, 257–261 (2014).

68. Gillespie, M. K., Humphreys, P., McMillan, H. J. & Boycott, K. M. Association of early-onset spasticity and risk for cognitive impairment with mutations at amino acid 499 in SPAST. *J. Child Neurol.* **33**, 329–332 (2018).

69. Barad, B. A. et al. EMRinger: side chain-directed model and map validation for 3D cryo-electron microscopy. *Nat. Methods* **12**, 943–946 (2015).

Author contributions

C.R.S. froze EM grids, collected and processed EM data and built atomic models. A.S. purified all proteins, performed AUC and ATPase assays. E.A.Z. performed severing assays. C.R.S., G.C.L. and A.R.M. interpreted structural models and wrote the manuscript.

Competing interests

The authors declare no competing interests.

Additional information

Methods

Protein expression and purification. Full-length *Drosophila melanogaster* spastin[6] (sequence ID NP_001303437.1) with a Walker B mutation (E583Q) was expressed in *Escherichia coli* BL21DE3 cells as a N-terminal glutathione *S*-transferase (GST) fusion and purified by affinity chromatography, followed by PreScission protease cleavage of the GST[70]. After cleavage with PreScission protease, spastin was further purified on a HiTrapQ chromatography column (subtractive step) followed by a MonoS column (GE Healthcare). Spastin eluted as two peaks that were collected separately. The purer spastin peak was concentrated to ~5 mg ml⁻¹ and injected on a Superdex 200 size exclusion column (GE Healthcare) in 20 mM HEPES pH 7.5, 300 mM KCl, 10 mM MgCl₂, 5 mM DTT, 5% glycerol. The sample was concentrated to 10 mg ml⁻¹, flash frozen in liquid nitrogen and stored at −80 °C after supplementing the glycerol concentration to 15%. For ATPase and severing assays, the gel filtration step was omitted and the protein was concentrated to 5 mg ml⁻¹ and buffer exchanged into 20 mM HEPES pH 7.5, 300 mM KCl, 10 mM MgCl₂, 5 mM DTT and 15% glycerol. Single-use aliquots were flash frozen in liquid nitrogen and stored at −80 °C. All structure-based point mutants were generated using Quickchange mutagenesis and subjected to the same purification protocol as the wild-type protein.

Analytical ultracentrifugation. AUC experiments were conducted in a ProteomeLab XL-I analytical ultracentrifuge (Beckman Coulter) using absorption optics. The spastin Walker B mutant was subjected to size exclusion chromatography in 20 mM HEPES, 300 mM KCl, 10 mM MgCl₂ and 1 mM tris(2carboxyethyl)phosphine (TCEP). The eluted protein was used for the preparation of AUC samples in the same buffer supplemented with 0.1 mM ATP. The sample was loaded into a 12 mm cell, placed in an AN-Ti rotor and equilibrated thermally in the ultracentrifuge. After thermal equilibrium was reached at rest at 10 °C, the rotor was accelerated to 45,000 r.p.m. and intensity scans at 280 nm were started immediately and collected until no further sedimentation boundary movement was observed. Data were analyzed in terms of continuous $c(s)$ distributions using the SEDFIT program[71]. All accepted fits had r.m.s. deviations less than 0.008. Partial specific volume and buffer parameters were calculated using Sednterp (http://rasmb.org/sednterp/). Sedimentation coefficient distributions were corrected to standard conditions at 20 °C in water, $s_{20,w}$. For the detection of spastin and peptide co-sedimentation, a VGSEEEEEEEEEE peptide was synthesized and purified by biosynthesis and then its N terminus was labeled with Atto488 using Atto488-NHS ester (Sigma-Aldrich, no. 41698) according to the manufacturer's protocol. After labeling, peptides were reverse phase HPLC purified. Experiments were performed for peptide (16.7 μM) alone and spastin (10 μM for the monomer or 1.67 μM for the hexamer) and excess peptide (16.7 μM). The samples were placed in the four-hole AN-Ti rotor and equilibrated thermally in the ultracentrifuge. After thermal equilibrium was reached at rest at 10 °C, the rotor was accelerated to 50,000 r.p.m. and the intensity scans at 280 nm and 483 nm were started immediately and collected until no further sedimentation boundary movement was observed. Data were analyzed in terms of continuous $c(s)$ distributions using the SEDFIT program. All accepted fits had r.m.s. deviations less than 0.008. Partial specific volume and buffer parameters were calculated using Sednterp. Sedimentation coefficient distributions were corrected to standard conditions at 20 °C in water, $s_{20,w}$. Modeling the 9.9 s peak as a monodisperse species gives statistically identical solutions, indicating that the 9.9 s peak is not a mixture of oligomers[72].

Sample preparation for electron microscopy. Spastin^{E583Q} (1.2 mg ml⁻¹) was incubated on ice for ~20 min in 20 mM HEPES buffer (pH 7.5) containing 300 mM KCl, 10 mM MgCl₂, 5 mM DTT, 1 mM ATP and 0.05% lauryl maltose neopentyl glycol (LMNG) detergent with and without 0.22 μM 1,500–5,500 molecular weight polyglutamate peptide (Sigma-Aldrich). Then 2.5 μl of sample was applied to a UltraAuFoil R1.2/1.3 300-mesh grid (Electron Microscopy Services) freshly plasma-cleaned using a Gatan Solarus (75% argon/2% oxygen atmosphere, 15 W for 7 s). Grids were manually blotted with filter paper (Whatman No.1) for ~4 s in a 4 °C cold room before plunge freezing in liquid ethane cooled by liquid nitrogen.

Electron microscopy data acquisition. All cryo-EM data were acquired using the Leginon automated data-acquisition program[73]. All image pre-processing (frame alignment, contrast transfer function (CTF) estimation, particle picking) were performed in real-time using the Appion image-processing pipeline during data collection[74]. Images were collected on a Thermo Fischer Talos Arctica operating at 200 keV, equipped with a Gatan K2 Summit DED, at a nominal magnification of ×36,000 corresponding to a physical pixel size of 1.15 Å per pixel. 2,534 videos (48 frames per video) were collected using an exposure time of 12 s with an exposure rate of 5.6 e⁻/pixel/s, resulting in a total dose of 52 e⁻/Å² (1.08 e⁻ per frame) with a nominal defocus range from −1.0 to −2.0 μm.

Image processing. A total of 564 images were used for automated particle picking using the Difference of Gaussians (DoG) picker to yield 92,387 particles[74]. CTFFIND4 was used for CTF estimation before extracting particles. Particles were Fourier-binned 4 × 4 and subjected to reference-free two-dimensional (2D) classification using multivariate statistical analysis and multi-reference alignment in the Appion pipeline. The best three classes representing end-on, tilted and side views were selected for template-based particle picking using FindEM resulting in 2,736,856 particle picks. The ~2.7 million particles picks were extracted unbinned and subjected to two rounds of reference-free 2D classification in cryoSPARC[75] to remove non-particles and poorly aligning particles in the data (Supplementary Fig. 3). Particles from exemplary classes (strong secondary structural features present in the 2D classes) comprised a subset of 1,259,553 particles. This subset then went on to reference-free ab initio model generation in cryoSPARC, resulting in an initial three-dimensional (3D) model. Homogeneous refinement resulted in a map with a reported resolution of ~3.4 Å. Some disordered density above the topmost protomer was observed, which we attributed to an off-register misalignment of a subset of particles relative to the majority register. 3D classification without alignment in RELION[76] using a tau-fudge value of 20 was successful in identifying the misaligned hexamers, which constituted 12% of the input particles. One class, which comprised 22% of the input particles, did not display the previously observed disordered density and was better ordered compared to the other five classes. 3D autorefinement in Relion with limited local and global search angles resulted in a ~4.2 Å map. We then used this map as a reference map for a heterogeneous refinement into two classes in cryoSPARC, using the original 1,259,553 particles that were kept after 2D classification. One class was significantly better ordered and was selected for an additional round of heterogenous refinement with two classes. One class was selected, based on visual inspection for quality of the reconstruction, for homogenous refinement resulting in a sharpened map of ~3.2 Å from 488,385 particles. This final reconstruction includes only 18% of the total particles initially selected from the micrographs. We attribute this to false particle picks, damaged particles from sample freezing, inaccurate defocus values, non-substrate-bound particles and sample heterogeneity. Notably, throughout the image processing of spastin, we did not observe any evidence of an additional conformational state other than the split lock-washer conformation, even at low resolution.

An additional data set of the spastin hexamer without the addition of the polyglutamate substrate resulted in a ~3.8 Å reconstruction with an unknown density within the central pore that resembled an unfolded polypeptide substrate (Supplementary Fig. 2). Similar densities have been observed for numerous AAA+ ATPase protein translocases[25,28,33]. Notably, of the ~300,000 particles selected from the images, only ~30,000 particles contributed to this final reconstruction. We were unable to identify the peptide species through mass spectrometry analysis due to its low abundance. We speculate that the unknown density is either due to a single low-abundant peptide species, or an average of many low-abundant peptides of differing sequences bound to spastin hexamers. Due to the presence of substrate density in the central pore of the hexamer, we speculated that substrate binding may have a stabilizing effect on the overall organization of the complex, and that a small minority of selected particles contained residual substrate that may have been retained through the protein purification. Indeed, pre-incubation of our spastin with polyglutamate peptide, known to bind to spastin and inhibit microtubule severing[20], increased the percentage of well-ordered hexamers observed in our dataset by ~twofold and resulted in a substantial improvement in resolution to ~3.2 Å of the substrate-bound spastin hexamer, which allowed atomic model building (Table 1 and above).

Atomic model building and refinement. A crystal structure of the *D. melanogaster* spastin monomer was used as a starting point[6] (PDB 3B9P) for modeling. Using Chimera[77], all loops and coils were deleted, and secondary structural elements were docked into the EM map. After one round of real-space refinement in Phenix[78], Coot[79] was used to rebuild coils and improve main chain and side chains. The rebuilt model was then used as the initial input for a multi-model-generating pipeline[80], which allowed for accessing model quality. Overall, 200 models were generated in Rosetta using the refined map and model, and the top 10 scoring models were selected for further model refinement using Phenix with a per-residue Cα r.m.s. deviations. Regions with poor model convergence were remodeled and refined. The Molprobity[81] server (http://molprobity.biochem.duke.edu/) and PDB validation service server (https://validate-rcsb-1.wwpdb.org/) were used to identify problem regions for subsequent correction in Coot. Residues 502–516 and 613–620 of protomer A are missing in the final model. The polyglutamate peptide was built de novo in Coot.

ATP hydrolysis assays. Basal ATP hydrolysis rates were measured at room temperature using the EnzChec Phosphate Assay Kit (Thermo Fisher Scientific) in 80 mM PIPES pH 6.8, 50 mM KCl, 1 mM EGTA, 2 mM MgCl₂ and 1 mM DTT for 50 nM spastin and point mutants. Initial rates were calculated from the linear portion of the reaction curve after addition of 2 mM ATP. ATPase rates were corrected by subtraction of the measured release of phosphate in the absence of ATP. Polyglutamate stimulated ATP hydrolysis rates were measured at room temperature in 20 mM HEPES pH 7.5, 50 mM KCl, 10 mM MgCl₂, 1 mM DTT and 2 mM ATP at 200 nM spastin and polyglutamate concentrations ranging from 0 to 100 μM. Stock solutions(100 mM) of polyglutamate (0.75–5.0 kDa) was made in water and adjusted to pH 7.5 with potassium hydroxide. Tenfold serial dilutions were made in water and added to the ATPase reaction, before the addition of ATP. Initial rates were calculated from the linear portion of the reaction curve. ATPase

rates were corrected by subtraction of the measured release of phosphate in the absence of ATP and polyglutamate.

Microtubule severing assays. Microtubules were polymerized from 2 mg ml⁻¹ bovine cycled brain tubulin (PurSolutions), 4% tetramethyl rhodamine labeled and 1% biotin-labeled porcine brain tubulin (Cytoskeleton). Microtubules were double-cycled with the slow-hydrolyzable GTP analog guanylyl (α,β)-methylene diphosphonate. The first polymerization was 1 h and the second polymerization overnight[82]. The microtubules were spun down at 126,000*g* using a TLA100 rotor (Beckman Coulter), re-suspended in warm BRB80 (80 mM K-PIPES pH 6.8, 1 mM MgCl₂ and 1 mM EGTA) and stored at 37 °C. Chambers for total internal reflection fluorescence (TIRF) microscopy were assembled as described previously[70]. Microtubules were immobilized in the chamber using 2 mg ml⁻¹ NeutrAvidin (Thermo Fisher Scientific) and imaged by TIRF microscopy in severing buffer containing BRB80, 2 mg ml⁻¹ casein, 9.1 mM 2-mercaptoethanol, 2.5% glycerol, 50 mM KCl, 2.5 mM MgCl₂, 1 mM ATP, 1% Pluronic F127 (Life Technologies) and oxygen scavengers[70]. Severing reactions were carried out using 20 nM full-length wild-type and mutants of *D. melanogaster* spastin. Severing was scored as previously described[20]. Images were acquired with a Nikon Ti-E microscope equipped with a ×60, 1.49 numerical aperture oil objective and a TI-TIRF adapter (Nikon) at 1 Hz with a 50 ms exposure time. Excitation was provided by a 561 nm laser (Agilent MLC) set to 20 mW before being coupled to the microscope by an optical fiber. The final pixel size for images was 90 nm. Image acquisition was carried out using Micro-Manager[83]. Image analysis was carried out in Fiji. Prism (Graphpad Inc.) was used for graphing and statistical analysis.

Quantification and data analysis. *N* is reported for all experiments in figure legends. Data in Fig. 4b,c were subjected to a Mann–Whitney statistical test.

Homology modeling. A human spastin hexamer homology model was generated using the online server SWISS-MODEL[84] (https://swissmodel.expasy.org/). Residues 228–617 of the M1 isoform (UniProt Q9UBP0) were used as a targeting sequence and our 3.2 Å atomic model of the *D. melanogaster* spastin was used as a template. Coordinates for the homology model are available as Supplementary Data Set 1.

Reporting Summary. Further information on research design is available in the Nature Research Reporting Summary linked to this article.

Data availability
Electron microscopy map and the top scoring model of five atomic models obtained from an EM multi-model pipeline have been deposited at the Electron Microscopy Data Bank and Protein Data Bank under accession numbers EMD-20226 and PDB 6P07, respectively. All data used in this study are available from the corresponding authors upon reasonable request.

References
70. Ziolkowska, N. & Roll-Mecak, A. In vitro microtubule severing assays. *Neurochem. Int.* **37**, 399–400 (2013).
71. Schuck, P. Size-distribution analysis of macromolecules by sedimentation velocity ultracentrifugation and Lamm equation modeling. *Biophys. J.* **78**, 1606–1619 (2000).
72. Brown, P. H., Balbo, A. & Schuck, P. Using prior knowledge in the determination of macromolecular size-distributions by analytical ultracentrifugation. *Biomacromolecules* **8**, 2011–2024 (2007).
73. Carragher, B. et al. Leginon: an automated system for acquisition of images from vitreous ice specimens. *J. Struct. Biol.* **132**, 33–45 (2000).
74. Voss, N. R., Yoshioka, C. K., Radermacher, M., Potter, C. S. & Carragher, B. DoG Picker and TiltPicker: software tools to facilitate particle selection in single particle electron microscopy. *J. Struct. Biol.* **166**, 205–213 (2009).
75. Punjani, A., Rubinstein, J. L., Fleet, D. J. & Brubaker, M. A. CryoSPARC: algorithms for rapid unsupervised cryo-EM structure determination. *Nat. Methods* **14**, 290–296 (2017).
76. Scheres, S. H. W. RELION: Implementation of a Bayesian approach to cryo-EM structure determination. *J. Struct. Biol.* **180**, 519–530 (2012).
77. Pettersen, E. F. et al. UCSF Chimera—a visualization system for exploratory research and analysis. *J. Comput. Chem.* **25**, 1605–1612 (2004).
78. Adams, P. D. et al. PHENIX: a comprehensive Python-based system for macromolecular structure solution. *Acta Crystallogr. D* **66**, 213–221 (2010).
79. Emsley, P. & Cowtan, K. Coot: model-building tools for molecular graphics. *Acta Crystallogr. D* **60**, 2126–2132 (2004).
80. Herzik, M. A., Fraser, J. S. & Lander, G. C. A Multi-model approach to assessing local and global cryo-EM map quality. *Structure* 27, 344–358 (2018).
81. Chen, V. B. et al. MolProbity: all-atom structure validation for macromolecular crystallography. *Acta Crystallogr. D* **66**, 12–21 (2010).
82. Gell, C. et al. in *Microtubule Dynamics. Methods in Molecular Biology (Methods and Protocols)* Vol. 777 (ed. Straube, A.) (Humana Press, 2011).
83. Edelstein, A. D. et al. Advance methods of microscope control using microManager software. *J. Biol. Methods* **1**, e10 (2014).
84. Waterhouse, A. et al. SWISS-MODEL: homology modelling of protein structures and complexes. *Nucleic Acids Res.* **46**, W296–W303 (2018).
85. Cardone, G., Heymann, J. B. & Steven, A. C. One number does not fit all: mapping local variations in resolution in cryo-EM reconstructions. *J. Struct. Biol.* **184**, 226–236 (2013).
86. Meng, E. C., Pettersen, E. F., Couch, G. S., Huang, C. C. & Ferrin, T. E. Tools for integrated sequence-structure analysis with UCSF Chimera. *BMC Bioinformatics* **7**, 1–10 (2006).

Corresponding author(s):	Antonina Roll-Mecak
Last updated by author(s):	05/15/2019

Reporting Summary

Nature Research wishes to improve the reproducibility of the work that we publish. This form provides structure for consistency and transparency in reporting. For further information on Nature Research policies, see Authors & Referees and the Editorial Policy Checklist.

Statistics

For all statistical analyses, confirm that the following items are present in the figure legend, table legend, main text, or Methods section.

n/a	Confirmed	
☐	☒	The exact sample size (n) for each experimental group/condition, given as a discrete number and unit of measurement
☐	☒	A statement on whether measurements were taken from distinct samples or whether the same sample was measured repeatedly
☐	☒	The statistical test(s) used AND whether they are one- or two-sided *Only common tests should be described solely by name; describe more complex techniques in the Methods section.*
☒	☐	A description of all covariates tested
☐	☒	A description of any assumptions or corrections, such as tests of normality and adjustment for multiple comparisons
☐	☒	A full description of the statistical parameters including central tendency (e.g. means) or other basic estimates (e.g. regression coefficient) AND variation (e.g. standard deviation) or associated estimates of uncertainty (e.g. confidence intervals)
☐	☒	For null hypothesis testing, the test statistic (e.g. F, t, r) with confidence intervals, effect sizes, degrees of freedom and P value noted *Give P values as exact values whenever suitable.*
☒	☐	For Bayesian analysis, information on the choice of priors and Markov chain Monte Carlo settings
☒	☐	For hierarchical and complex designs, identification of the appropriate level for tests and full reporting of outcomes
☒	☐	Estimates of effect sizes (e.g. Cohen's d, Pearson's r), indicating how they were calculated

Our web collection on statistics for biologists contains articles on many of the points above.

Software and code

Policy information about availability of computer code

Data collection	Leginon, Appion, Micromanager
Data analysis	CTFFIND4, cryoSPARC, Relion, Coot, Phenix, Chimera, Molprobity, SWISS-MODEL, Fiji, Prism

For manuscripts utilizing custom algorithms or software that are central to the research but not yet described in published literature, software must be made available to editors/reviewers. We strongly encourage code deposition in a community repository (e.g. GitHub). See the Nature Research guidelines for submitting code & software for further information.

Data

Policy information about availability of data

All manuscripts must include a data availability statement. This statement should provide the following information, where applicable:
- Accession codes, unique identifiers, or web links for publicly available datasets
- A list of figures that have associated raw data
- A description of any restrictions on data availability

All data described are available and PDB ID will be provided before publication.

Field-specific reporting

Please select the one below that is the best fit for your research. If you are not sure, read the appropriate sections before making your selection.

☒ Life sciences ☐ Behavioural & social sciences ☐ Ecological, evolutionary & environmental sciences

For a reference copy of the document with all sections, see nature.com/documents/nr-reporting-summary-flat.pdf

Life sciences study design

All studies must disclose on these points even when the disclosure is negative.

Sample size	NA
Data exclusions	none
Replication	All data were replicated independently
Randomization	NA
Blinding	NA

Reporting for specific materials, systems and methods

We require information from authors about some types of materials, experimental systems and methods used in many studies. Here, indicate whether each material, system or method listed is relevant to your study. If you are not sure if a list item applies to your research, read the appropriate section before selecting a response.

Materials & experimental systems

n/a	Involved in the study
☒ ☐	Antibodies
☒ ☐	Eukaryotic cell lines
☒ ☐	Palaeontology
☒ ☐	Animals and other organisms
☒ ☐	Human research participants
☒ ☐	Clinical data

Methods

n/a	Involved in the study
☒ ☐	ChIP-seq
☒ ☐	Flow cytometry
☒ ☐	MRI-based neuroimaging